An Autocatalytic Mechanism for NiFe-Hydrogenase: Reduction to Ni(I) Followed by Oxidative Addition

Sten O. Nilsson Lill* and Per E. M. Siegbahn*

Department of Physics, Albanova, and Department of Biochemistry and Biophysics, Arrhenius Laboratory, Stockholm University, SE-106 91 Stockholm, Sweden

Received June 29, 2008; Revised Manuscript Received December 10, 2008

ABSTRACT: The mechanism for H_2 cleavage in NiFe-hydrogenase has been reinvestigated with large models using both hybrid DFT by itself, or in a QM/MM scheme following the ONIOM approach. Heterolytic cleavage, with one hydrogen ending up as a bridging hydride and one as a proton on a cysteine ligand, was found to have a barrier slightly too high to be compatible with measured catalytic turnover rates. Alternative mechanisms were therefore investigated. In the finally suggested mechanism, heterolytic cleavage is used only as an initial step to generate a complex with nickel in oxidation state Ni(I). In the following cycles, H_2 is instead cleaved on nickel using an oxidative addition mechanism with a lower barrier. It was found that the ONIOM results for the reaction mechanism in NiFe-hydrogenase needed to be corrected by large model DFT results to be more reliable. This was mainly an effect of overestimation of polarization effects of the QM region by the MM region due to the particular treatment of the electrostatic interactions and the use of a standard (nonpolarizable) force field.

Hydrogenases are enzymes designed to reversibly cleave dihydrogen into protons and electrons

$$H_2 \leftrightarrow 2H^+ + 2e^- \quad (1)$$

They are classified by specifying the transition metal content of their active sites into three main classes, the NiFe (*1*−*3*), the FeFe (*4, 5*), and the iron−sulfur cluster free hydrogenases (*6*−*9*). The NiFe enzymes are primarily used for hydrogen oxidation and the FeFe enzymes for proton reduction. The iron−sulfur cluster free hydrogenases activate dihydrogen for use in catabolic processes within the cell but do not catalyze proton reduction or dihydrogen oxidation. Certain organisms also contain dihydrogen-sensing hydrogenases, which regulate dihydrogen oxidation and/or proton reduction in these organisms (*10, 11*).

The X-ray structure of the active site of NiFe-hydrogenase for *Desulfovibrio fructosovorans* (*2*) is shown in Figure 1.

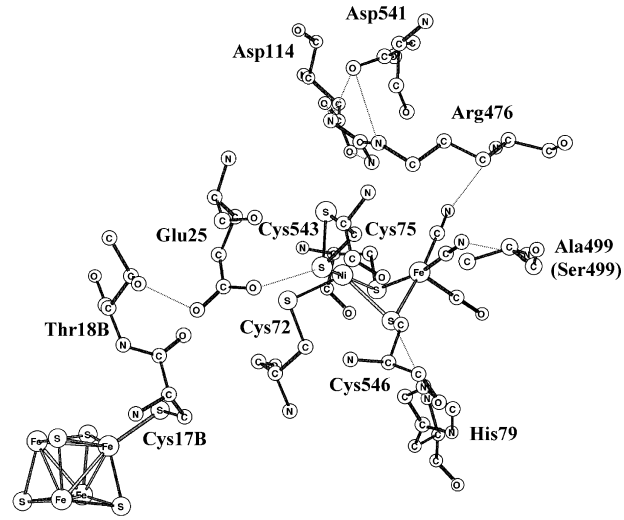

FIGURE 1: X-ray structure of the active site for NiFe-hydrogenase from *D. fructosovorans*.

There are four cysteinate ligands, two of them bridging nickel and iron, and two of them terminally bound to nickel. Note that two positions of the sulfur of Cys543 are shown from the X-ray analysis. Iron has in addition three diatomic ligands, of which two are cyanides and one is a carbonyl, very unusual for a biological metal complex. Another unusual aspect of the active site is that so many of the nearest amino acids, not bound to the metals, are charged. There is one positive arginine, hydrogen bonding to two negative aspartates. There are also one nearby glutamic acid and one histidine, both of which could be charged. As will be discussed below, a modeling of this type of complex is very challenging. For example, in a QM/MM model it is required to model strong electrostatic effects and also hydrogen bonding between charged groups described at the MM level,

* To whom correspondence should be addressed. S.O.N.L.: e-mail, stenil@physto.se; telephone, +46-8-16 12 65; fax, +46-8-55 37 86 01. P.E.M.S.: e-mail, ps@physto.se; telephone, +46-8-16 12 63; fax, +46-8-55 37 86 01.

[1] Abbreviations: QM, quantum mechanics; MM, molecular mechanics; EPR, electron paramagnetic resonance; ENDOR, electron−nuclear double resonance; DFT, density functional theory; B3LYP, Becke's three-parameter hybrid functional using Lee−Yang−Parr correlation functional; ONIOM, our own N-layered integrated molecular orbital with molecular mechanics; ESP, electrostatic potential; PES, potential energy surface; ZPE, zero-point energy; NBO, natural bond order; PDB, Protein Data Bank; EE, electronic embedding; UV, ultraviolet; MCD, magnetic circular dichroism; MR-MP2, multireference Møller−Plesset theory truncated at second order; CASSCF, complete active space self-consistent field; TS, transition state; Ni-A, catalytically inactive oxidized state; Ni_a-S, catalytically active EPR-silent state; Ni_a-SR, catalytically active EPR-silent reduced state; Ni_a-C*, catalytically active EPR-active state; Ni_a-R*, catalytically active EPR-active reduced state; Ni_a-X*, catalytically active EPR-active intermediate state (asterisks indicate an EPR-active enzyme state).

10.1021/bi801218n CCC: $40.75
Published on Web 01/12/2009

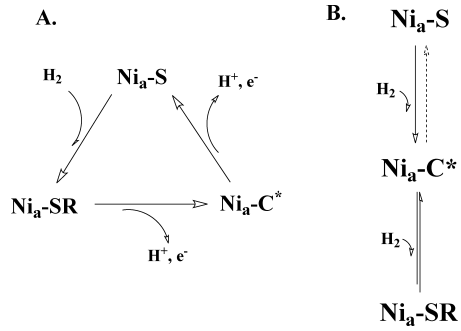

FIGURE 2: Two different types of catalytic cycles for NiFe-hydrogenases, suggested by experiments.

with charged groups described at the QM level, which may give rise to rather large errors using a standard approach.

The catalytic cycle of NiFe-hydrogenases is commonly illustrated by a scheme such as the one in Figure 2A (*12, 13*). It contains the three intermediate states observed experimentally, Ni_a-C*, Ni_a-S, and Ni_a-SR. Ni_a-C* is the EPR-active resting state, which on the basis of its X-ray structure (*2*) and recent ENDOR results (*14*−*16*) has been suggested to have a bridging hydride between the metals. The EPR-silent Ni_a-SR state is reached by reduction of Ni_a-C*, while Ni_a-S, which is also EPR-silent, is obtained by oxidation. To complete the cycle, Ni_a-SR can be reached by adding dihydrogen to Ni_a-S. Several other states have been observed under varying conditions, but these will not be discussed in this paper.

A few additional aspects of the active cycle of NiFe-hydrogenase have been implicated from experiments, apart from what is shown in Figure 2A. First, since the gas channel from the surface ends at nickel, this metal has been suggested as the binding site for dihydrogen (*17, 18*). The fact that the inhibitors CO (*19*) and O_2H^- (*20, 21*) bind at nickel is another indication that this could be the binding site for dihydrogen. Second, since the consensus mechanism for hydrogenases involves heterolytic cleavage of dihydrogen, a base is required, which has been suggested to be a terminal cysteine (Cys543 in *D. fructosovorans*) on nickel. One reason for this suggestion is that the sulfur of this cysteine is replaced with selenium in a common class of NiFe-hydrogenases (*2*), indicating a special role for this cysteine in the mechanism. This cysteine is also located close to the suggested proton transfer pathway (*22*) and has a high temperature factor in the X-ray studies, indicating a conformational flexibility. A water molecule bound to iron has also been suggested as a base, from a combined EPR and DFT study (*23, 24*).

An interesting alternative scenario to the one in Figure 2A, shown in Figure 2B, has also been suggested (*25*). The main difference between these mechanisms is that Ni_a-S does not participate in the active cycle. Instead, catalysis starts only after an initial reaction between Ni_a-S and dihydrogen, where Ni_a-C* is created. Ni_a-C* is then only in equilibrium with Ni_a-SR during turnover (*26*). The structural implications of this suggestion have not been completely clear, but it has been suggested that a bridging hydride may be present all the time during catalysis (*25, 27*).

Even though experimental techniques have given many hints about the mechanism of NiFe-hydrogenase, a full characterization has not been possible. This is, for example, illustrated by the fact that the two quite different scenarios, shown in panels A and B of Figure 2, are still both valid alternatives at present. One reason for this difficulty is that some intermediates are likely to be so short-lived that they cannot be detected experimentally. This means that theoretical modelings, where a short-lived species is not a problem, must also be used if the correct mechanism should be found. Very soon after the first X-ray structure, DFT studies were started and have continued since then. After the first decade of studies, it appeared that essential agreement was reached from these DFT studies with a mechanism that basically follows the one in Figure 2A (see refs *28* and *29* and references cited therein). Most DFT studies so far have agreed that dihydrogen binds to iron, in contrast to what has been suggested by the enzyme experiments discussed above. Dihydrogen binding to iron is instead in line with what is known from many organometallic complexes, where binding to a low-spin metal is a common feature (*30*). Even though the energy difference between the binding to nickel and iron is rather small, it seems unlikely that DFT should fail to predict the correct binding site, provided that the chemical model is adequate. DFT studies also agreed that it is not possible to activate dihydrogen if a bridging hydride is already present. The barrier is so high that it should be fairly safe to exclude this possibility. This is in agreement with isotope exchange studies showing that the hydride present is exchangeable and not positioned between iron and nickel (*10*). The preferred heterolytic cleavage mechanism was in most studies found to be one in which one hydrogen ends up as a bridging hydride and the other as a proton on a terminal cysteine, in broad agreement with the suggestions made on the basis of experiments. The most serious disagreement between the DFT studies has concerned the spin state of the EPR-inactive states as either a singlet or a triplet (*31*−*33*), and whether a NiFe(III,II) or NiFe(II,II) state is the active species in the heterolytic cleavage (*31, 35*). At that stage, with basic agreement on most issues, a serious modeling problem was detected for the oxidized states (*36*). It turned out that even rather large models of the active site failed to reproduce the correct binding mode of the hydroperoxide anion in Ni-A. Instead of a side-on binding to nickel as observed in the X-ray structures (*20, 21*), a bridging end-on structure was obtained with a quite large energetic preference of more than 10 kcal/mol. This result has clearly cast severe doubts on the other DFT predictions of the mechanism, and it was therefore decided that a renewed investigation should be made with a model much larger than that used before. The results of these model studies of both QM and QM/MM type will be presented here.

METHODS AND MODELS

All QM geometry optimizations were performed at the B3LYP level with a double-ζ quality basis set using Jaguar 5.5. Open-shell systems (doublets and triplets) were treated using unrestricted DFT. Transition states were optimized with a few key distances frozen from the corresponding fully optimized ONIOM result (see below). Single-point energy calculations on these structures were performed with a large basis set. To evaluate solvation effects, the self-consistent reaction field method as implemented in Jaguar was employed using a polarized double-ζ basis set.

Two-layer ONIOM optimizations were performed using Gaussian 03. The QM portion of the system (~30 atoms) was treated using B3LYP/lanl2dz, including an effective core potential on both nickel and iron. The rest of the system was treated using AMBER (parm96.dat) as implemented in Gaussian 03. The partitioning of the two layers is displayed in the Supporting Information. Partial charges for the QM atoms needed for the ONIOM calculations were taken from an ESP calculation (UB3LYP/LANL2DZ) on a DFT-optimized model system of an apoenzyme consisting of 115 atoms. To investigate the influence of the partial charges for the QM atoms, new ESP charges were calculated for these atoms from either DFT- or ONIOM-optimized structures of Ni_a-C* and for the TS for oxidative addition for a system consisting of 137 atoms (see below). Reoptimizations were performed, and it was found that the energy difference between these reoptimized structures was less than 1 kcal/mol. This suggests that the structures resulting from the different optimizations employing different ESP charges are very similar. This was also confirmed by visual inspections and small rms deviations (0.0156 Å). Since the final energies reported are taken from electronic embedding (EE) calculations, the only influence of the ESP charges is in the optimization and thus the converged structures on which the EE calculations are performed.

Singlet states were investigated as either closed-shell or open-shell systems using the broken-symmetry approach as implemented in Gaussian 03. Stability tests were performed on triplets and singlets to search for more stable wave functions. All ONIOM-optimized geometries were characterized as minima or saddle points on the potential energy surface (PES) by using the sign of the eigenvalues of the force constant matrix obtained from a frequency calculation which also gave the zero-point energy (ZPE) for each compound. Transition states with one imaginary frequency were confirmed to describe the correct movement on the PES by a mode analysis. Free energy calculations were performed under standard conditions (298 K and 1 atm). Single-point energies on ONIOM-optimized structures were calculated using B3LYP/cc-pvtz(-f) on main atoms and LACV3P+ for nickel and iron. The solvation calculations used the lacvp* basis set, a dielectric constant of 4.0, and a probe radius of 1.40 Å. The model used for these calculations is the 127-atom DFT model, described below. As a test of the DFT functional, single-point calculations were also performed by reducing the amount of HF exchange to 15% (B3LYP*). The influence of polarization on the QM part from the MM residues was added by performing single-point calculations, including electronic embedding. NBO analysis was performed with either NBO 5.0 as implemented in Jaguar or NBO 3.1 as implemented in Gaussian 03. Starting coordinates and residue numberings were taken from a crystal structure of NiFe-hydrogenase (PDB entry 1YQW), after removal of the O_2H^- ligand and remutation of Ala499 to Ser499 to model the wild-type structure of the enzyme.

The catalytic cycle of NiFe-hydrogenase involves not only the cleavage of the dihydrogen bond but also the removal of two (H^+,e^-) couples. By the present methodology, only relative energies for these removals can be accurately calculated. To obtain absolute values, the total driving force of the cycle is estimated and the results are fitted to this value. The value chosen for the driving force is −1.0 kcal/mol, as in the previous study (*29*), since it should be small without any unnecessary waste of energy. It should also be rather easily reversible, requiring a small driving force. The accuracy of this choice is estimated to be a few kilocalories per mole, and any change in this order has only minor effects on the individual energies and does not change the conclusions drawn here. Further details of this procedure can be found in the previous review (*29*).

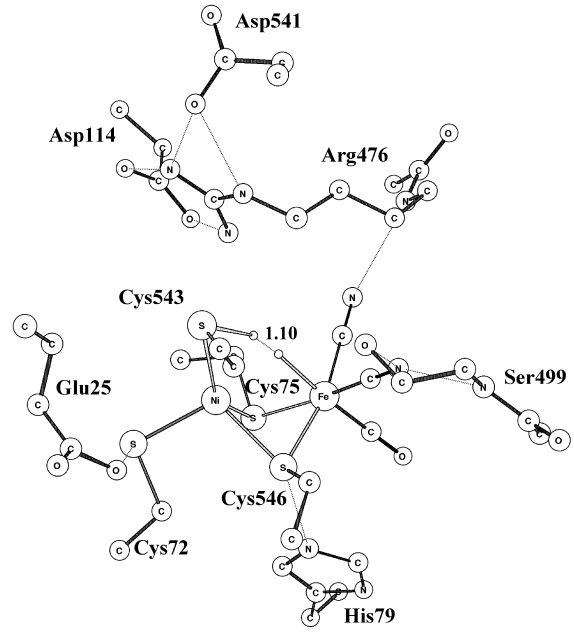

FIGURE 3: Model with 137 atoms showing the transition state for heterolytic cleavage of the H−H bond. Hydrogen atoms on the amino acids have been omitted for the sake of clarity.

RESULTS

A major reason for this reinvestigation of the mechanism of NiFe-hydrogenase was, as mentioned in the introductory section, the modeling problems encountered for the peroxide Ni-A state (*36*). It was shown that a model with as many as 114 atoms gave an energetically quite strongly preferred geometry for a structure which is not in agreement with experiments. Therefore, in this study, a combination of both QM and QM/MM models is used which together give the right preference for Ni-A. The DFT model includes 137 atoms and is shown in Figure 3. It contains, besides the direct ligands, also the side chains of Arg476, Glu25, His79, Asp114, Asp541, and Ser499 and some parts of the backbones. Glu25 was chosen as neutral and His79 as protonated, on the basis of the previous study, and the other amino acids were taken with their normal charge states. The details of how this model was chosen for Ni-A will be presented elsewhere (*37*).

The new models were first used to study the mechanism, previously suggested from DFT calculations (*28, 29*), and this will be described in Heterolytic Cleavage Mechanism. This mechanism will be termed heterolytic cleavage. As a model test, an ONIOM calculation was performed for the same 137-atom model that was used in the DFT calculations. This ONIOM model has 30 atoms in the QM part and the remaining 107 atoms in the MM part. The results for a much larger 363-atom ONIOM model, again with 30 atoms in the QM part but now with 333 atoms in the MM part, are also

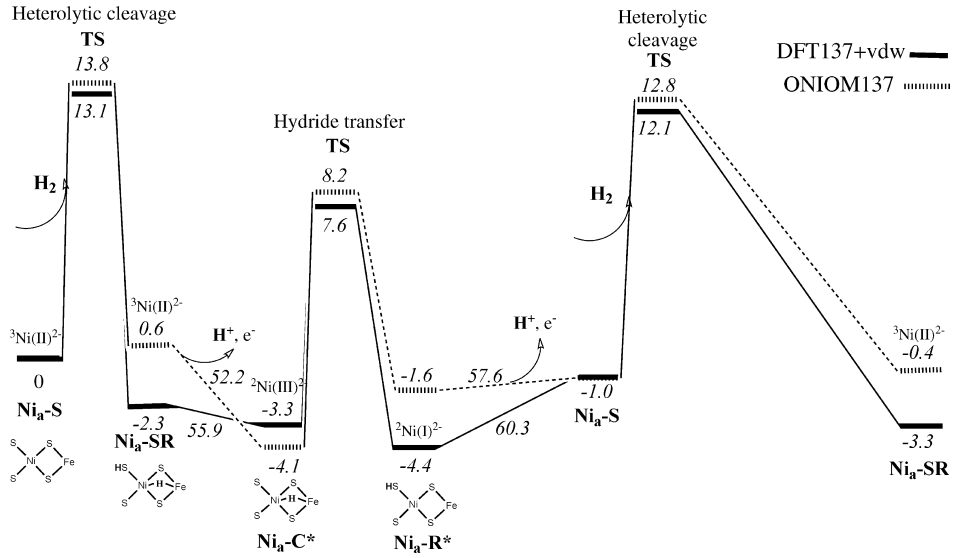

FIGURE 4: DFT and ONIOM results for the heterolytic cleavage mechanism using the 137-atom model. The values in italics are the values for the binding energy of a gas-phase H atom [(H^+,e^-) couple].

presented. The strategy employed here is to use the results of all these three models to make a better prediction. The difference for the same 137-atom model between the DFT and ONIOM results, excluding the small van der Waals contributions (see the Supporting Information), is used to yield a correction to the ONIOM procedure. The corrections are mainly due to a deficiency in describing electrostatic effects between the QM and MM parts. The ONIOM corrections used below are on the order of 1−5 kcal/mol, depending on the specific state, and are used to correct the results for the large 363-atom ONIOM model. However, it should be noted that for other partitionings between the QM and MM parts, the corrections can be much larger. In the discussion below, the final results are instead described as ONIOM-corrected DFT results, which is exactly the same thing as described above.

In the process of the renewed investigation of the mechanism, the idea of a quite different mechanism arose. This mechanism will be termed oxidative addition, and the results are presented in Oxidative Addition Mechanism.

Heterolytic Cleavage Mechanism. Essentially all DFT studies on NiFe-hydrogenase have been in agreement on the main features of the mechanism. Dihydrogen binds to iron and is cleaved heterolytically with one hydrogen ending up as a bridging hydride and the other hydrogen as a proton on a base. Most studies also agree on the favored base as the terminally bound Cys543. In the earliest study, the bridging Cys546 was instead suggested as the base (*38*), but later studies showed that if His79 is protonated this pathway becomes less favorable (*31*). There is also one study that suggests an external water as the base (*23, 24*). These studies have been recently reviewed (*29*). In support of this mechanism, isotope exchange studies have been interpreted as indicating a heterolytic cleavage mechanism (*39*). It was therefore natural to start this investigation with this mechanism. The results for the DFT calculations using the 137-atom model are shown in Figure 4, together with the results using ONIOM for the same model. To simplify the comparisons below, the (small) van der Waals contributions from the ONIOM calculations are added to the DFT results in the figure.

The potential curve of these DFT results is in many ways very similar to the previous one (*29*). As in earlier studies, H_2 binds to iron, and the optimized transition state is shown in Figure 3. The H−H distance is 1.10 Å, and the spin population on nickel is 1.42 [cc-pvtz(-f), B3LYP*]. For the Ni_a-S reactant, the spin is also 1.42. Glu25 has moved its hydrogen bond from Cys543 to Cys72 in the TS to allow greater Cys543 flexibility. The rate-limiting barrier is 16.5 kcal/mol compared to the previous one of 15.7 kcal/mol (*29*). The value of 16.5 kcal/mol is obtained as the energy difference between the lowest state in the first cycle (−4.4 kcal/mol for Ni_a-R*) and the heterolytic cleavage barrier in the second cycle (12.1 kcal/mol) and is why part of this cycle has been included in the figure.

The immediate product of the heterolytic cleavage is state Ni_a-SR with a nickel spin population of 1.44, 2.3 kcal/mol lower than the reactant Ni_a-S at the DFT level. Ni_a-SR has a bridging hydride and a protonated Cys543. At this stage, an H atom [(H^+,e^-) couple] has to leave the complex, and state Ni_a-C* with a spin population of 0.90 and oxidation state Ni(III) on nickel is formed. The computed energy to reach a gas-phase H atom is 55.9 kcal/mol, which is translated into an exergonic reaction by 1.0 kcal/mol using the procedure described in Methods and Models, by assuming a small driving force of −1.0 kcal/mol for the whole process. To move from Ni_a-C* to Ni_a-R*, the hydride should move from its bridging position between the metals to Cys543. The product Ni_a-R* was found also in the previous study (*31*) and turns out to be of key importance for the second mechanism discussed below. The barrier for hydride transfer at the DFT level is 10.9 kcal/mol, making it substantially smaller than the barrier for heterolytic cleavage. Ni_a-R* has a nickel spin population of 0.94 and is the most reduced state of nickel in the catalytic cycle with oxidation state Ni(I). Iron stays in oxidation state II during the entire cycle. To return to the starting point for the heterolytic cleavage, state Ni_a-S, another H atom has to leave the complex. The computed energy to reach a gas-phase H atom is 60.3 kcal/mol at the DFT level, translated to an endergonic process of 3.4 kcal/mol.

There are three low-lying states in the cycle, Ni_a-SR, Ni_a-

C*, and Ni_a-R*, at −2.3, −3.3, and −4.4 kcal/mol, respectively. These energy differences are so small that the accuracy of DFT is not high enough to conclusively determine which one is actually lowest. While Ni_a-C* has been unambiguously characterized spectroscopically, Ni_a-R* seems to require more careful attention to be detected. However, at temperatures below 160 K, an EPR-active intermediate state in *Acidithiobacillus ferrooxidans* has been characterized by Lubitz et al. (*40, 41*). This light-insensitive state was found to have EPR signals similar to those of the light-induced Ni-L state which has been suggested to be in a Ni(I) state with the hydride removed from the bridging position. Thus, Ni_a-R* is a strong candidate for being this intermediate state. Similarly, Bernhard et al. has for *Ralstonia eutropha* observed a transient species with EPR signals reminiscent of the intermediate state observed by the Lubitz group (*11*). The geometric structures are schematically shown in the figure. In the previous study, Ni_a-C* was the lowest state at −4.1 kcal/mol, which is also the suggested experimental resting state. There are a few rather large deviations to the previous results. The barrier for hydride transfer presented here is 11.0 kcal/mol compared to the previous one of only 3.5 kcal/mol. In the hydride transfer, the side chain of Cys543 rotates to accept the proton, and its ability to move therefore affects the barrier. In this study, the backbone atoms of Cys543 were held fixed from the X-ray structure, whereas in the previous study, Cys543 as a whole was given more freedom to move, resulting in an artificially low barrier for hydride transfer.

The ONIOM results for the same model, also shown in Figure 4, have a similar shape of the potential curve. However, the deviations to the DFT results are not negligible and have consequences later for the conclusions about the mechanism. For example, the minimum of Ni_a-C* is 0.8 kcal/mol deeper and is now lowest in energy, the TS point for heterolytic cleavage is 0.7 kcal/mol higher, and the hydride transfer barrier from Ni_a-C* is 1.4 kcal/mol higher. The overall rate-limiting barrier is 16.9 kcal/mol compared to the DFT barrier of 16.5 kcal/mol. As described above, these differences will be considered to be due to deficiencies of the QM/MM procedure and are used to correct the final estimate of the potential curve.

In the course of this study, several different models were used for the DFT calculations, and the results were all compared to ONIOM calculations for the same model. The model shown in Figure 3 is the one which gave the smallest deviations between DFT and ONIOM. For an initial model lacking Asp541, with 127 atoms, the deviations were considerably larger than in the model presented here. For example, the ONIOM minimum for Ni_a-SR is as much as 8.2 kcal/mol higher than at the DFT level of theory and the hydride transfer 6.1 kcal/mol higher. These results are a strong warning against accepting QM/MM results without a careful analysis and verification that QM/MM appropriately describes not only the reactant state structures but also relative energies along the reaction path. However, when applied properly, QM/MM methods have undoubtedly contributed to our understanding of enzyme mechanisms and in numerous investigations have been shown to give reliable and useful insights for other enzymes (*42*−*44*). Addition of Asp541 makes the reaction energy between Ni_a-S and Ni_a-SR more exothermic, using either DFT (−6.2 kcal/mol) or ONIOM (−11.5 kcal/mol). The effect on the reaction energy is thus ∼5 kcal/mol stronger (more negative) using ONIOM than DFT. This suggests that the polarization from the negative charge of Asp541 on the QM region, described by the electronic embedding approach, is overestimated. Such overpolarization effects have been observed previously (*45*) and are normally handled by scaling or removing charges close to the QM/MM boundary. To further verify the polarization effect in this system, the optimized structure from the ONIOM137 system was used but all charges in Asp541 were set to zero. This led to an increase of the reaction energy of 7.1 kcal/mol which thus reflects the polarization effect from Asp541 on the QM region. Similarly, removing Asp541 completely gave a corresponding effect of 7.3 kcal/mol, showing that the contributions from other MM terms are small. By an alternative approach, where the charges on Asp541 were scaled by a factor of 0.25 corresponding to a dielectric constant of 4, the effect from Asp541 decreases from −11.5 to −6.0 kcal/mol. This is in very good agreement with the effect calculated using DFT of −6.2 kcal/mol and appears to be a possible way of handling the overpolarization experienced in QM/MM calculations. Further studies on this topic are at present underway.

A comparison of the results for the 137-atom ONIOM model, discussed above, with the larger 363-atom model is shown in Figure 5. The deviations between these curves are of the same size as the ones between the DFT and the 137-atom ONIOM curves in Figure 4. In this case, the deviations should not be artificial but due to real chemical effects from the region of the protein not included in the smaller model. The largest effects occur for the heterolytic cleavage TS point with 2.9 kcal/mol and the hydride transfer TS point with 2.7 kcal/mol. The rate-limiting barriers are 16.9 kcal/mol for the small ONIOM and 18.8 kcal/mol for the large one. The hydride transfer barrier is also somewhat higher with the larger model, 14.0 kcal/mol compared to 12.3 kcal/mol. Clearly, the region of the protein outside the 137-atom model has not been evolutionarily optimized for heterolytic cleavage.

The final best estimate of the potential curve for the heterolytic cleavage mechanism is shown in Figure 6. This curve is constructed from the results of all three models by taking the DFT curve and adding the difference between the small and large ONIOM curves. Since the van der Waals effects have already been added to the DFT curve, these will not enter into the correction of the DFT curve. The largest correction to the DFT results appears for the heterolytic cleavage barrier, where the TS point is raised from 13.1 to 16.0 kcal/mol, an increase of 2.9 kcal/mol. Since the resting state, Ni_a-R*, for the corrected curve is also raised, by 1.8 kcal/mol, the rate-limiting barrier increases by only 1.1 kcal/mol from 16.5 to 17.6 kcal/mol. The hydride transfer barrier is also raised, by 0.9 kcal/mol from the resting state, to 11.9 kcal/mol. Altogether, the final best estimate curve is in reasonable agreement with experimental observations [barrier of 13 kcal/mol (*22*)], although with a rate which is too slow to be entirely satisfactory, even considering that an overly high barrier is a common feature for B3LYP (and B3LYP*).

Before the second mechanism is discussed, some remarks should be made about the electronic structure character of the intermediates involved. The first comment concerns the spin states. The question of whether Ni(II) is in its low-spin (singlet) or high-spin (triplet) state has been given different

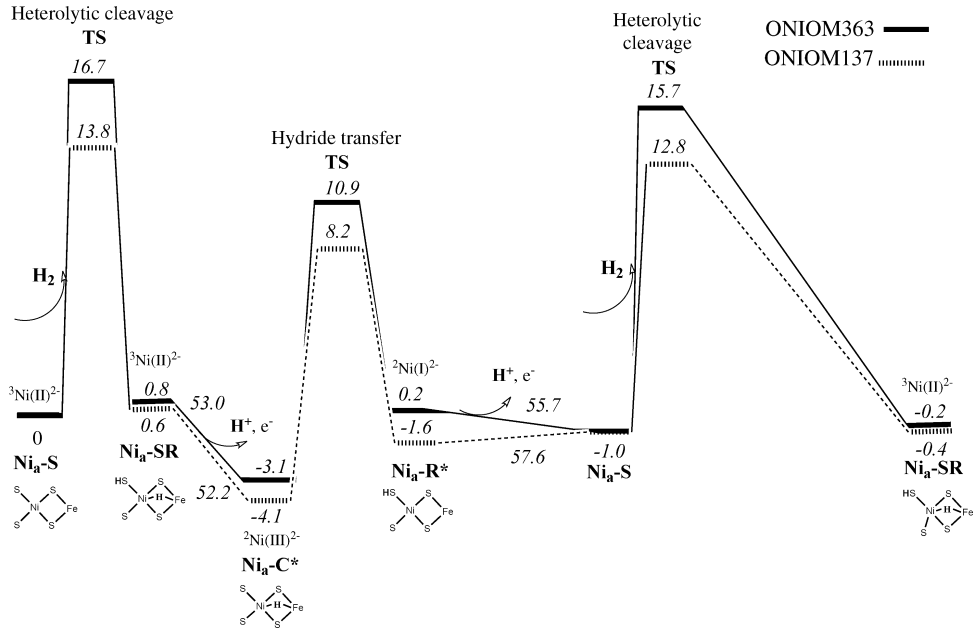

FIGURE 5: ONIOM results for the heterolytic cleavage mechanism using the 137- and 363-atom models.

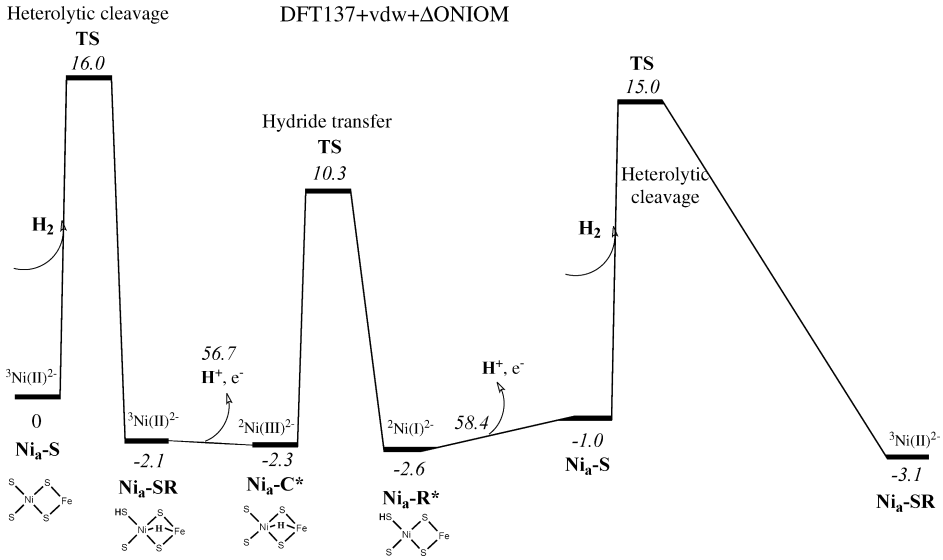

FIGURE 6: Final best estimate of the potential curve for the heterolytic mechanism. The DFT results are corrected with the ΔONIOM results.

answers depending on the experimental technique used or computational method employed. Parallel mode EPR (*46*), saturation magnetization (*47*), and UV−visible MCD studies (*48*) suggest singlet (diamagnetic) spin states. A triplet state has later been suggested on the basis of B3LYP calculations (*32*) and L-edge X-ray adsorption spectroscopy (*49*). A DFT analysis has also been made using functionals with different amounts of exact exchange, and the conclusion was that the singlet and triplet states were almost degenerate for the model of the active site used (*33*). The model system used differs from the core of these models by having one of the terminal cysteines protonated already in the Ni_a-S state. More recently, the singlet−triplet splitting for the Ni_a-S state was investigated using DFT, MR-MP2, and CASSCF on both DFT-optimized model systems and ONIOM-optimized enzyme models (*34*). MP2 and DFT, and surprisingly even the B3LYP functional, were found to favor the singlet state, while CASSCF favors the high-spin triplet state. To shed further light on this problem, the singlet−triplet splitting was analyzed using B3LYP* energies on the initial DFT127-optimized model of both Ni_a-S and the TS for H_2 cleavage. The calculated B3LYP* energy differences of 7.1 kcal/mol between the triplet and open-shell singlet in Ni_a-S and 7.4 kcal/mol for the TS clearly suggest that the high-spin state is preferred and that no spin crossing occurs along the reaction. The closed-shell singlet solution was found to be even less stable than the open-shell singlet. To test additional points on the potential energy surface, the Ni_a-S H_2 complex was also analyzed. The ONIOM363 results suggest that the triplet is 4.8 kcal/mol more stable than the singlet. The difference between these and previous results probably stems from the size of the QM model and the approach, used in this study, to fix atoms in the backbone of the residues to mimic the active site of the enzyme. In another study, it has been found that the geometry for the triplet state is more similar to the structure in the active site than the geometry for the singlet state (*32*). It may therefore be of some

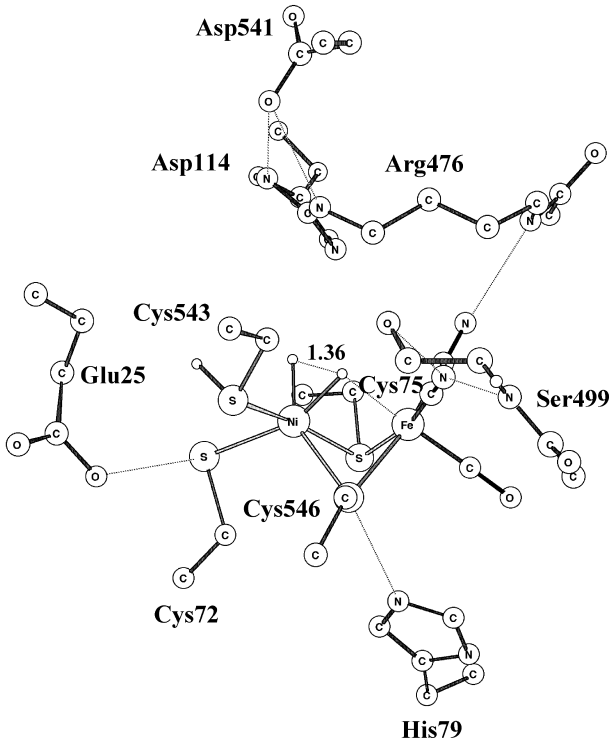

FIGURE 7: Model with 137 atoms showing the transition state for oxidative addition. Hydrogen atoms on the amino acids have been omitted for the sake of clarity.

importance to keep the structure of the system rather rigid to have a good active site model.

Oxidative Addition Mechanism. There are several reasons for continuing searching for alternative mechanisms to the heterolytic cleavage discussed above. One reason is that the final barrier for the heterolytic mechanism is still rather high. Another reason comes from indications from some experiments (*25, 26*) that Ni_a-S and Ni_a-C* should not be in equilibrium during the catalytic cycle (see Figure 2B). This led to suggestions that a heterolytic cleavage should occur with a bridging hydride always present in the catalytic cycle. However, attempts to find a low-energy pathway of this type all failed (*29*). An interesting state in the context of a new mechanism is instead Ni_a-R*, since it has nickel in oxidation state Ni(I). In principle, this allows oxidative addition to form Ni(III), which is already known to be an accessible state. The structure of Ni_a-R* is also rather open which should allow a favorable interaction between nickel and H_2. As already mentioned, some experiments have favored an interaction between H_2 and nickel rather than one with iron (*17, 18*). Attempts to find a catalytic cycle that goes through oxidative addition on nickel were therefore made. The transition state obtained at the DFT level is shown in Figure 7. Compared to the TS for the heterolytic mechanism, Cys543 is protonated. The H−H distance is 1.36 Å, and the spin population on nickel is 0.81. In comparison, the population is 0.94 for the Ni_a-R* reactant.

The DFT and ONIOM results for the oxidative addition using the 137-atom model are shown in Figure 8. To reach the Ni_a-R* reactant for the oxidative addition, an initial heterolytic cleavage has to occur, and this part of the mechanism is therefore also shown in the figure. To make a comparison between heterolytic cleavage and oxidative addition, the second cycle of heterolytic cleavage is shown as well. The oxidative addition leads to an energy plateau at ~14 kcal/mol, which after several intermediates reaches the Ni_a-R* state, which is the starting point for the next catalytic cycle. The mechanism suggested for oxidative addition thus consists of an initial heterolytic cleavage followed by oxidative addition for all following cycles. This type of mechanism is termed autocatalytic since the active site itself in an initial step forms the active catalyst (Ni_a-R*) for the following steps. In this mechanism, states Ni_a-S and Ni_a-SR are not in equilibrium with each other, in line with what is suggested by some experiments (*25, 26*) and shown in Figure 2B. However, the computed energy barrier for this mechanism is ~2 kcal/mol higher at the DFT level than that for just continuing with heterolytic cleavage.

To return to the catalytic cycle after the oxidative addition is rather complicated with several intermediates. Directly after the oxidative addition TS, a state here termed Ni_a-X* is formed with nickel in oxidation state III and with two hydrides, one bridging and one terminal. The reason the energy is higher for Ni_a-X* than for the preceding TS point is that the corrections added after the TS optimization, from zero-point, thermal, and dielectric effects, reversed the energy ordering of these points. The energetic effect of these corrections should be interpreted as moving the TS toward Ni_a-X*. Ni_a-SR can then be reached from Ni_a-X* by sending an electron to the iron−sulfur cluster acceptor and a proton to the bulk. This is essentially a downhill process with probably only a very small barrier. From Ni_a-SR, state Ni_a-C* can be reached by another release of an (H^+,e^-) couple. From Ni_a-C*, the starting point for the next oxidative addition, Ni_a-R*, is then reached by a hydride transfer. Both these steps are only shown for the first heterolytic cycle in the figure but are, of course, identical for the oxidative addition cycle.

The general shape of the ONIOM curve using the same 137-atom model is rather similar to the DFT results. Again, as in the heterolytic mechanism, there are errors in the ONIOM procedure, now of up to 6 kcal/mol, which need to be taken into account for the final corrections. The largest error occurs for the TS point for oxidative addition, where ONIOM is 6.3 kcal/mol too high. To test the energy dependence of the optimized geometry, single-point calculations using ONIOM on DFT137-optimized structures were performed. It was found that the TS for oxidative addition could be lowered by 3.2 kcal/mol using DFT-optimized structures. The barrier for oxidative addition is more similar, with 18.6 kcal/mol at the DFT level and 21.7 kcal/mol at the ONIOM level.

When the large ONIOM is compared to the small ONIOM, an important difference can be noticed for the two different mechanisms (see Figure 9). While the large ONIOM increases the barriers for heterolytic cleavage, there is a notable decrease in the barriers for oxidative addition. For the TS for oxidative addition, there is a reduction of 4.8 kcal/mol, and for the intermediate Ni_a-X*, it is 2.6 kcal/mol. For heterolytic cleavage, there is instead an increase of 2.9 kcal/mol. It is clear that the selection of amino acids in the region outside the 137-atom core differentially favors oxidative addition. For the other intermediates in the diagram, the differences between the large and small ONIOMs are much smaller.

When the differential effects between the large and small

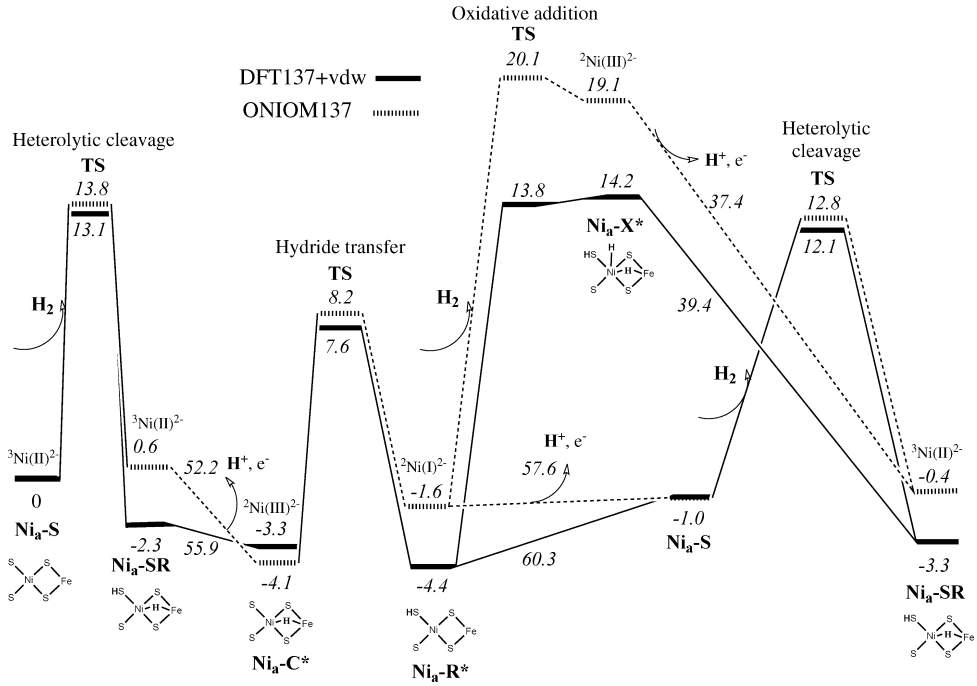

FIGURE 8: DFT and ONIOM results for the combined heterolytic cleavage and oxidative addition mechanisms using the 137-atom model.

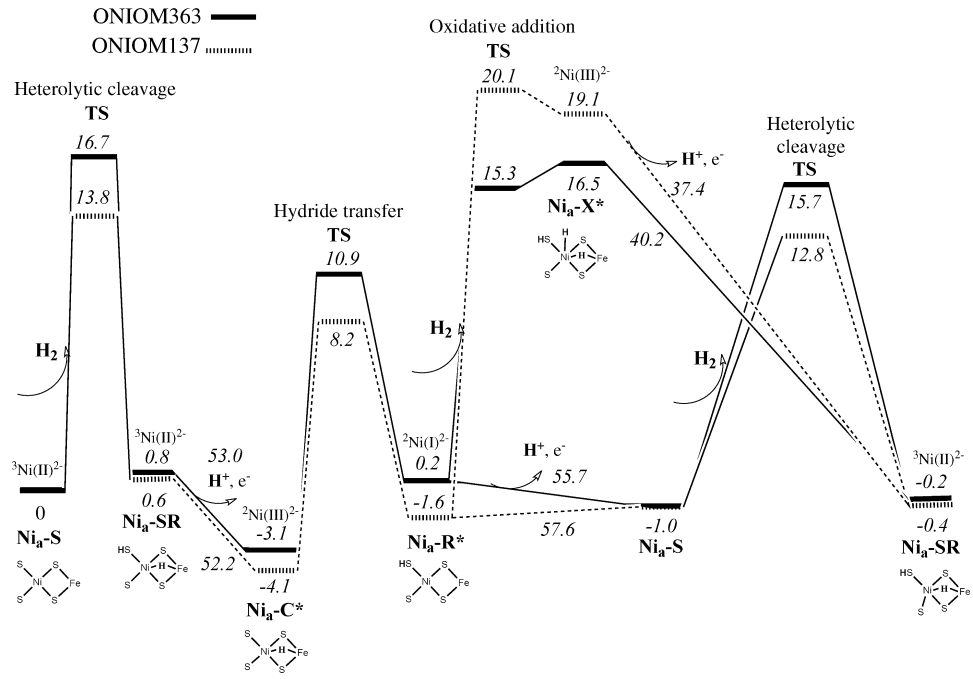

FIGURE 9: ONIOM results for the combined heterolytic cleavage and oxidative addition mechanisms using the 137- and 363-atom models.

ONIOMs are added to the DFT results, the diagram in Figure 10 is obtained. The interesting result is that now oxidative addition is slightly preferred over heterolytic cleavage. The rate-limiting barrier for oxidative addition is 14.2 (=2.6 + 11.6) kcal/mol, while it is 17.6 (2.6 + 15.0) kcal/mol for heterolytic cleavage. The activation barrier for the oxidative addition of 14.2 kcal/mol is in good agreement with the experimental value of 13 kcal/mol (*22*). There are two main sources of error for B3LYP barriers. The first one is the self-interaction error which tends to give overly low barriers, and the other is a lack of nondynamical correlation which has the opposite effect. For redox-active enzymes, it has been shown that B3LYP often gives barriers which are slightly too high (*50*). Bearing in mind that the activation barrier in this study is extrapolated from a QM/ONIOM approach, we must consider the 1 kcal/mol deviation satisfactory. The conclusion is therefore that only the first cycle will use heterolytic cleavage, to create intermediate Ni_a-R* which has Ni(I) and is suitable for oxidative addition in all the following cycles. This type of combined mechanism is in line with the one in Figure 2B, suggested by experiments (*25, 26*), where Ni_a-S is not part of the catalytic cycle after the first H_2 addition.

As expected, entropy effects play a major role in the activation barriers for H_2 cleavage. The combined effect of zero-point, entropy, and other temperature effects is 7.7 kcal/

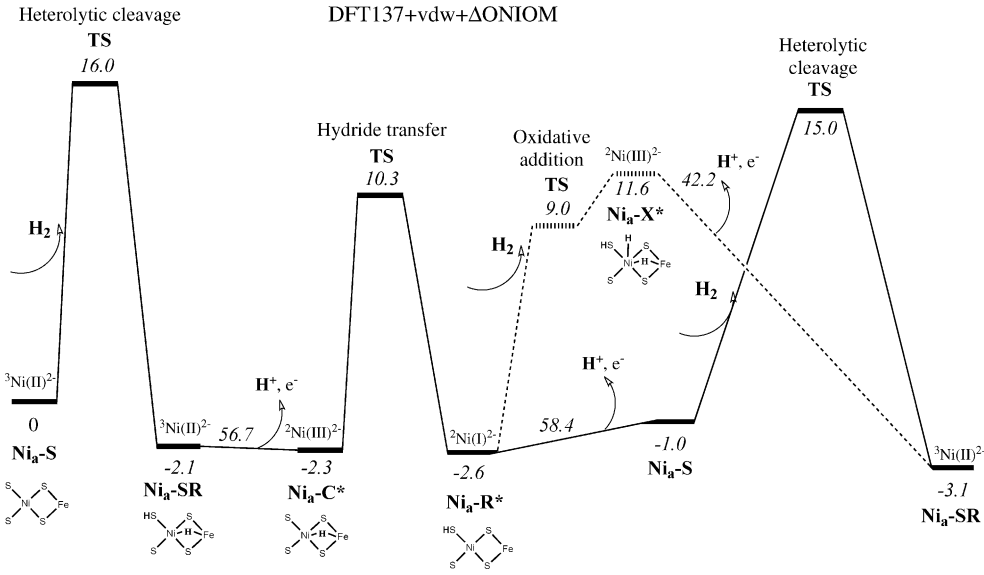

FIGURE 10: Final best estimate of the potential curve for the combined heterolytic cleavage and oxidative addition mechanisms. The DFT results are corrected with the ΔONIOM results.

mol for the barrier for heterolytic cleavage. For the oxidative addition part, the effect is even larger with 8.3 kcal/mol for the TS point and 9.7 kcal/mol for Ni_a-X*. The larger effect for Ni_a-X* is one reason this point at the end is higher than the preceding TS point; large basis set and dielectric effects are other.

The isotope exchange studies, which have been interpreted as an indication of heterolytic cleavage (*10*), do not exclude a mechanism that proceeds via an oxidative addition. What has been observed experimentally are two nonequivalent hydrogens, interpreted as one proton and one hydride appearing after a heterolytic cleavage, and these have different rate constants for exchange with D_2O. However, the exchange reaction would take place from either Ni_a-SR, Ni_a-C*, or Ni_a-R* in a manner independent of mechanism, since these states appear both for heterolytic cleavage and for oxidative addition.

The spin population analysis indicates that Fe is in a low-spin state throughout the whole catalytic cycle. During the heterolytic cleavage reaction, where Ni(II) is in its triplet state, most of the spin is located on Ni. In the reactant state Ni_a-S, some of the spin is delocalized out on the sulfur atoms of the two terminal cysteinates coordinating Ni. This contrasts the product state (Ni_a-SR), where the spin distribution is more evenly distributed over the three negatively charged cysteinates, with a small preference for the two bridging cysteinates. However, the terminal cysteinate which accepts the proton has only a small net spin density. In Ni_a-C*, where nickel is in a Ni(III) state, the spin population on Ni is 0.90, somewhat smaller than in the previous states. Transfer of the hydride to the terminal cysteineate, giving Ni_a-R* with nickel in a Ni(I) state, increases the spin on nickel by a small amount to 0.94. From the spin density analysis alone, it is thus difficult to assess nickel as Ni(I) or Ni(III). Analysis of the product of the oxidative addition (Ni_a-X*) where nickel is reoxidized to Ni(III) reveals that the spin density on nickel is reduced to 0.78. The two hydrogens in H_2 in the TS for oxidative addition have charges of −0.17 and −0.03, respectively, indicating two hydrides rather than one proton and one hydride. In the product state (Ni_a-X*), these charges are −0.23 and −0.06, respectively. Only a fraction of spin density is observed on these hydrides.

CONCLUSIONS

The mechanism for H_2 cleavage by NiFe-hydrogenase has been reinvestigated with models larger than those previously used. At the DFT level, the largest model has 137 atoms, in which all backbone atoms were held fixed from the X-ray structure. At the QM/MM level, calculations were performed using the ONIOM scheme for a model with 363 atoms, of which 30 atoms were described at the QM level. To calibrate the accuracy of the QM/MM results, calculations were performed with ONIOM also for the 137-atom model (with 30 QM atoms). The differences between the DFT and ONIOM results for the 137-atom model (after subtraction of van der Waals effects) were considered as errors of the QM/MM procedure and were used to correct the ONIOM results for the 363-atom model. The errors for the 137-atom model were found to be in the range of 1−6 kcal/mol. For smaller models, the error was sometimes as large as 8 kcal/mol. An analysis of these errors shows that the main origin is an exaggeration of electrostatic effects. The effects can be damped by scaling the charges with the dielectric constant or perhaps by including more water molecules in the model.

The DFT-corrected ONIOM scheme was first applied to the standard model of heterolytic cleavage of H_2 with results rather similar to those obtained previously. Even though the results are in reasonable agreement with experiments, the barrier is somewhat high and other mechanisms were therefore also tried. One of these mechanisms was found to be particularly interesting. This is an oxidative addition on a Ni(I) state (Ni_a-R*) appearing as an intermediate in the heterolytic cycle. At the highest level of theory (see Figure 10), oxidative addition was found to have a barrier 3.4 kcal/mol lower than the one for heterolytic cleavage. Since half a cycle of heterolytic cleavage is needed to generate Ni_a-R*, the mechanism is termed autocatalytic. The suggested mechanism is in line with a mechanism suggested by experiments shown in Figure 2B, where Ni_a-S is not in equilibrium with Ni_a-SR once catalysis has started (*25, 26*).

An interesting aspect of this mechanism is that H_2 cleavage occurs on nickel, as suggested by some experiments (*17, 18*). Previous studies by DFT, all for mechanisms which had heterolytic cleavage, always found H_2 activation on iron.

SUPPORTING INFORMATION AVAILABLE

QM/MM partitioning, ESP charges, van der Waals radii of active site atoms, and van der Waals correction terms along the PES. This material is available free of charge via the Internet at http://pubs.acs.org.

REFERENCES

1. Przbyla, A. E., Robbins, J., Menon, N., and Peck, H. D. (1992) Structure-Function Relationships among the Nickel-Containing Hydrogenases. *FEMS Microbiol. Rev. 88*, 109–113.
2. Volbeda, A., Martin, L., Cavazza, C., Matho, M., Faber, B., Roseboom, W., Albracht, S., Garcin, E., Rousset, M., and Fontecilla-Camps, J. (2005) Structural Differences between the Ready and Unready Oxidized States of [NiFe] Hydrogenases. *J. Biol. Inorg. Chem. 10*, 239–249.
3. Teixeira, M., Moura, I., Xavier, A. V., Huynh, B. H., DerVartanian, D. V., Peck, H. D., Jr., LeGall, J., and Moura, J. J. G. (1985) Electron-Paramagnetic Resonance Studies on the Mechanism of Activation and the Catalytic Cycle of the Nickel-Containing Hydrogenase from *Desulfovibrio gigas*. *J. Biol. Chem. 260*, 8942–8950.
4. Nicolet, Y., Lemon, B. J., Fontecilla-Camps, J. C., and Peters, J. W. (2000) A Novel FeS Cluster in Fe-Only Hydrogenases. *Trends Biochem. Sci. 25*, 138–143.
5. Peters, J. W. (1999) Structure and Mechanism of Iron-Only Hydrogenases. *Curr. Opin. Struct. Biol. 9*, 670–676.
6. Lyon, E. J., Shima, S., Buurman, G., Chowdhuri, S., Batschauer, A., Steinbach, K., and Thauer, R. K. (2004) UV-A/Blue-Light Inactivation of the 'Metal-Free' Hydrogenase (Hmd) from Methanogenic Archaea: The Enzyme Contains Functional Iron after All. *Eur. J. Biochem. 271*, 195–204.
7. Berkessel, A., and Thauer, R. K. (1995) On the Mechanism of Catalysis by a Metal-Free Hydrogenase from Methanogenic Archaea: Enzymatic Transformation of H-2 without a Metal and Its Analogy to the Chemistry of Alkanes in Superacidic Solution. *Angew. Chem., Int. Ed. 34*, 2247–2250.
8. Thauer, R. K., Klein, A. R., and Hartmann, G. C. (1996) Reactions with Molecular Hydrogen in Microorganisms: Evidence for a Purely Organic Hydrogenation Catalyst. *Chem. Rev. 96*, 3031–3042.
9. Lyon, E. J., Shima, S., Boecher, R., Thauer, R. K., Grevels, F.-W., Bill, E., Roseboom, W., and Albracht, S. P. J. (2004) Carbon Monoxide as an Intrinsic Ligand to Iron in the Active Site of the Iron-Sulfur-Cluster-Free Hydrogenase H-2-Forming Methylene-tetrahydromethanopterin Dehydrogenase As Revealed by Infrared Spectroscopy. *J. Am. Chem. Soc. 126*, 14239–14248.
10. Vignais, P. M., Dimon, B., Zorin, N. A., Tomiyama, M., and Colbeau, A. A. (2000) Characterization of the Hydrogen-Deuterium Exchange Activities of the Energy-Transducing Hupsl Hydrogenase and H-2-Signaling Hupuv Hydrogenase in *Rhodobacter capsulatus*. *J. Bacteriol. 182*, 5997–6004.
11. Bernhard, M., Buhrke, T., Bleijlevens, B., De Lacey, A. L., Fernandez, V. M., Albracht, S. P. J., and Friedrich, B. (2001) The H-2 Sensor of *Ralstonia eutropha*: Biochemical Characteristics, Spectroscopic Properties, and Its Interaction with a Histidine Protein Kinase. *J. Biol. Chem. 276*, 15592–15597.
12. De Lacey, A. L., Fernandez, V. M., Rousset, M., and Cammack, R. (2007) Activation and inactivation of hydrogenase function and the catalytic cycle: Spectroelectrochemical studies. *Chem. Rev. 107*, 4304–4330.
13. Armstrong, F. A., and Albracht, S. P. J. (2005) [NiFe]-hydrogenases: Spectroscopic and electrochemical definition of reactions and intermediates. *Philos. Trans. R. Soc. London, Ser. A 363*, 937–954.
14. Brecht, M., van Gastel, M., Buhrke, T., Friedrich, B., and Lubitz, W. (2003) Direct Detection of a Hydrogen Ligand in the [NiFe] Center of the Regulatory H-2-Sensing Hydrogenase from *Ralstonia eutropha* in Its Reduced State by HYSCORE and ENDOR Spectroscopy. *J. Am. Chem. Soc. 125*, 13075.
15. Foerster, S., Stein, M., Brecht, M., Ogata, H., Higuchi, Y., and Lubitz, W. (2003) Single Crystal EPR Studies of the Reduced Active Site of [NiFe] Hydrogenase from *Desulfiovibrio vulgaris* Miyazaki F. *J. Am. Chem. Soc. 125*, 83–93.
16. Foerster, S., van Gastel, M., Brecht, M., and Lubitz, W. (2005) An Orientation-Selected ENDOR and HYSCORE Study of the Ni-C Active State of *Desulfovibrio vulgaris* Miyazaki F Hydrogenase. *J. Biol. Inorg. Chem. 10*, 51.
17. Montet, Y., Amara, P., Volbeda, A., Vernede, X., Hatchikian, E. C., Field, M. J., Frey, M., and Fontecilla-Camps, J. C. (1997) Gas Access to the Active Site of Ni-Fe Hydrogenases Probed by X-Ray Crystallography and Molecular Dynamics. *Nat. Struct. Biol. 4*, 523–526.
18. Volbeda, A., and Fontecilla-Camps, J. C. (2003) The Active Site and Catalytic Mechanism of NiFe Hydrogenases. *Dalton. Trans.,* 4030–4038.
19. Ogata, H., Mizoguchi, Y., Mizuno, N., Miki, K., Adachi, S.-I., Yasuoka, N., Yagi, T., Yamauchi, O., Hirota, S., and Higuchi, Y. (2002) Structural Studies of the Carbon Monoxide Complex of [NiFe]Hydrogenase from *Desulfovibrio vulgaris* Miyazaki F: Suggestion for the Initial Activation Site for Dihydrogen. *J. Am. Chem. Soc. 124*, 11628–11635.
20. Volbeda, A., Martin, L., Cavazza, C., Matho, M., Faber, B. W., Roseboom, W., Albracht, S. P. J., Garcin, E., Rousset, M., and Fontecilla-Camps, J. C. (2005) Structural Differences between the Ready and Unready Oxidized States of [NiFe] Hydrogenases. *J. Biol. Inorg. Chem. 10*, 239–249.
21. Ogata, H., Hirota, S., Nakahara, A., Komori, H., Shibata, N., Kato, T., Kano, K., and Higuchi, Y. (2005) Activation Process of [NiFe] Hydrogenase Elucidated by High-Resolution X-ray Analyses: Conversion of the Ready to the Unready State. *Structure 13*, 1635–1642.
22. Frey, M., and Fontecilla-Camps, J. C. (2001) Nickel-Iron Hydrogenases. In *Handbook of Metalloproteins* (Messerschmidt, A., Huber, R., Poulos, T., and Wieghardt, K., Eds.) Vol. 2, pp 880−896, John Wiley & Sons, Chichester, U.K.
23. Stein, M., and Lubitz, W. (2004) Relativistic DFT Calculation of the Reaction Cycle Intermediates of [NiFe] Hydrogenase: A Contribution to Understanding the Enzymatic Mechanism. *J. Inorg. Biochem. 98*, 862–877.
24. Stein, M., and Lubitz, W. (2002) Quantum Chemical Calculations of [NiFe] Hydrogenase. *Curr. Opin. Chem. Biol. 6*, 243–249.
25. Kurkin, S., George, S. J., Thorneley, R. N. F., and Albracht, S. P. J. (2004) Hydrogen-Induced Activation of the [NiFe]-Hydrogenase from *Allochromatium vinosum* As Studied by Stopped-Flow Infrared Spectroscopy. *Biochemistry 43*, 6820–6831.
26. Roberts, L. M., and Lindahl, P. A. (1995) Stoichiometric Reductive Titrations of *Desulfovibrio gigas* Hydrogenase. *J. Am. Chem. Soc. 117*, 2565–2572.
27. Amara, P., Volbeda, A., Fontecilla-Camps, J. C., and Field, M. J. (1999) A Hybrid Density Functional Theory Molecular Mechanics Study of Nickel-Iron Hydrogenase: Investigation of the Active Site Redox States. *J. Am. Chem. Soc. 121*, 4468–4477.
28. Bruschi, M., Zampella, G., Fantucci, P., and De Gioia, L. (2005) DFT Investigations of Models Related to the Active Site of [NiFe] and [Fe] Hydrogenases. *Coord. Chem. Rev. 249*, 1620–1640.
29. Siegbahn, P. E. M., Tye, J. W., and Hall, M. B. (2007) Computational Studies of [NiFe] and [FeFe] Hydrogenases. *Chem. Rev. 107*, 4414–4435.
30. Kubas, G. J. (2001) *Metal Dihydrogen and σ-Bond Complexes: Structure, Theory and Reactivity*, Kluwer Academic/Plenum Publishers, Dordrecht, The Netherlands.
31. Siegbahn, P. E. M. (2004) Proton and Electron Transfers in [NiFe] Hydrogenase. *Adv. Inorg. Chem. 56*, 101–125.
32. Fan, H.-J., and Hall, M. B. (2002) High-Spin Ni(II), a Surprisingly Good Structural Model for [NiFe] Hydrogenase. *J. Am. Chem. Soc. 124*, 394–395.
33. Bruschi, M., De Gioia, L., Zampella, G., Reiher, M., Fantucci, P., and Stein, M. (2004) A Theoretical Study of Spin States in Ni-S-4 Complexes and Models of the [NiFe] Hydrogenase Active Site. *J. Biol. Inorg. Chem. 9*, 873–884.
34. Jayapal, P., Robinson, D., Sundararajan, M., Hillier, I. H., and McDouall, J. J. W. (2008) High Level ab Initio and DFT Calculations of Models of the Catalytically Active Ni-Fe Hydrogenases. *Phys. Chem. Chem. Phys. 10*, 1734–1738.
35. Pardo, A., de Lacey, A., Fernandez, V. M., Fan, Y., and Hall, M. B. (2006) Density Functional Study of the Catalytic Cycle of Nickel-Iron [NiFe] Hydrogenases and the Involvement of High-Spin Nickel(II). *J. Biol. Inorg. Chem. 11*, 286–306.

36. Siegbahn, P. E. M. (2007) Hybrid Density Functional Study of the Oxidized States of NiFe-Hydrogenase. *C. R. Chim. 10*, 766–774.
37. Nilsson Lill, S., and Siegbahn, P. E. M. (2008)A DFT and QM/MM Study of the Ni-A State of NiFe-Hydrogenase: Refined Models for Prediction of the Correct Binding Mode, manuscript submitted for publication.
38. Pavlov, M., Siegbahn, P. E. M., Blomberg, M. R. A., and Crabtree, R. H. (1998) Mechanism of H-H Activation by Nickel-Iron Hydrogenase. *J. Am. Chem. Soc. 120*, 548–555.
39. Vignais, P. M. (2005) H/D Exchange Reactions and Mechanistic Aspects of the Hydrogenases. *Coord. Chem. Rev. 249*, 1677–1690.
40. Trofantchouk, O. (2001) Center of [NiFe] Hydrogenases. EPR, ENDOR and FTIR Studies Ph.D. Thesis, Technischen Universität Berlin.
41. Schröder, O., Bleijlevens, B., de Jongh, T. E., Chen, Z., Li, T., Fischer, J., Forster, J., Friedrich, C. G., Bagley, K. A., Albracht, S. P. J., and Lubitz, W. (2007) Characterization of a cyanobacterial-like uptake [NiFe] hydrogenase: EPR and FTIR spectroscopic studies of the enzyme from *Acidithiobacillus ferrooxidans*. *J. Biol. Inorg. Chem. 12*, 212–233.
42. Friesner, R. A. (2005) Modeling Polarization in Proteins and Protein−ligand Complexes: Methods and Preliminary Results. *Adv. Protein Chem. 72*, 79–104.
43. Riccardi, D., Schaefer, P., Yang, Y., Yu, H., Ghosh, N., Prat-Resina, X., König, P., Li, G., Xu, D., Guo, H., Elstner, M., and Cui, Q. (2006) Development of Effective Quantum Mechanical/Molecular Mechanical (QM/MM) Methods for Complex Biological Processes. *J. Phys. Chem. B 110*, 6458–6469.
44. Senthilkumar, K., Mujika, J. I., Ranaghan, K. E., Manby, F. R., Mulholland, A. J., and Harvey, J. N. (2008) Analysis of Polarization in QM/MM Modelling of Biologically Relevant Hydrogen Bonds. *J. R. Soc. Interface 5*, S207−S216.
45. Vreven, T., Byun, K. S., Komaromi, I., Dapprich, S., Montgomery, J. A., Jr., Morokuma, K., and Frisch, M. J. (2006) Combining Quantum Mechanics Methods with Molecular Mechanics Methods in ONIOM. *J. Chem. Theory Comput. 2*, 815–826.
46. Dole, F., Fournel, A., Magro, V., Hatchikian, E. C., Bertrand, P., and Guigliarelli, B. (1997) Nature and Electronic Structure of the Ni-X Dinuclear Center of *Desulfovibrio gigas* Hydrogenase. Implications for the Enzymatic Mechanism. *Biochemistry 36*, 7847–7854.
47. Wang, C. P., Franco, R., Moura, J. J. G., Moura, I., and Day, E. P. (1992) The Nickel Site in Active *Desulfovibrio baculatus* [NiFeSe] Hydrogenase Is Diamagnetic: Multifield Saturation Magnetization Measurement of the Spin State of Ni(II). *J. Biol. Chem. 267*, 7378–7380.
48. Kowal, A. T., Zambrano, I. C., Moura, I., Moura, J. J. G., LeGall, J., and Johnsson, M. K. (1988) Electronic and Magnetic Properties of Nickel-Substituted Rubredoxin: A Variable-Temperature Magnetic Circular-Dichroism Study. *Inorg. Chem. 27*, 1162–1166.
49. Wang, H., Ralston, C. Y., Patil, D. S., Jones, R. M., Gu, W., Verhagen, M., Adams, M., Ge, P., Riordan, C., Marganian, C. A., Mascharak, P., Kovacs, J., Miller, C. G., Collins, T. J., Brooker, S., Croucher, P. D., Wang, K., Stiefel, E. I., and Cramer, S. P. (2000) Nickel L-Edge Soft X-ray Spectroscopy of Nickel-Iron Hydrogenases and Model Compounds: Evidence for High-Spin Nickel(II) in the Active Enzyme. *J. Am. Chem. Soc. 122*, 10544–10552.
50. Siegbahn, P. E. M. (2006) The Performance of Hybrid DFT on Mechanisms Involving Transition Metal Complexes in Enzymes. *J. Biol. Inorg. Chem. 11*, 695–701.

BI801218N